DOI: 10.1021/ma1025175

Macromolecules
ARTICLE

Formation of Mesomorphic Domains and Subsequent Structural Evolution during Cold Crystallization of Poly(trimethylene terephthalate)

Wei-Tsung Chuang,*,† Wen-Bin Su,† U-Ser Jeng,*,† Po-Da Hong,*,‡ Chun-Jen Su,† Chiu-Hun Su,† Yen-Chih Huang,† Kuei-Fen Laio,† and An-Chung Su§

†*National Synchrotron Radiation Research Center, Hsinchu 30076, Taiwan,* ‡*Department of Materials Science and Engineering, National Taiwan University of Science and Technology, Taipei 10607, Taiwan, and* §*Department of Chemical Engineering, National Tsing Hua University, Hsinchu 30013, Taiwan*

Received November 4, 2010; Revised Manuscript Received January 10, 2011

ABSTRACT: Preordering behavior of poly(trimethylene terephthalate) (PTT) upon cold crystallization was revealed via in situ simultaneous small/wide-angle X-ray scattering and differential scanning calorimetry (SAXS/WAXS/DSC) as well as time-resolved Fourier transform infrared (FTIR) spectroscopy. In the induction stage prior to the appearance of WAXS crystalline peaks, changes in the low-q (0.005−0.03 $Å^{-1}$) range of SAXS profiles suggested the formation of mesomorphic domains (with a linear dimension ∼18 nm). Parallel DSC and FTIR results indicated respectively that the preordering involved a trace amount of exothermic heat prior to discernible *trans*-to-*gauche* conformation change. Subsequently observed were the growth of these mesomorphic domains to a size ≈50 nm and the accompanying emergence of nanocrystalline grains (of dimensions of several nanometers) via a more localized nucleation-and-growth route. The final ripened structure hence comprised a percolated network of mesomorphic domains filled with dispersed nanocrystallites. Hierarchical evolutions of the large mesomorphic domains and the small nanocrystallites with crystallization time were correlated with WAXS-determined crystallinity development and DSC-revealed endothermic events. Transitions from the amorphous to mesomorphic domains and the mesomorphic to crystalline domains are illustrated quantitatively. The formation of large mesomorphic domains in the induction stage of crystallization and their influences on the subsequent crystallization are discussed in terms of liquid−liquid phase separation and gel formation.

Introduction

With combined physical properties of nylons and other aromatic polyesters for excellent elastic recovery, poly(trimethylene terephthalate) (PTT) is a promising material for versatile applications as engineering plastics and textile fibers.[1−3] In the past decade, melt crystallization behavior, morphological characteristics, and properties of PTT-based materials have been extensively reported.[4−8] More recently, cold crystallization of PTT has drawn considerable attention for its intriguing gelation-related crystallization behavior and practical use of tailored morphology of specific properties from deeply supercooled/kinetically trapped amorphous PTT in processes such as melt spinning.

In a previous report,[9] the early stage of PTT cold crystallization was shown to be dominated by the emergence of finely dispersed sheaf-like crystallites, leading to gelation-like dynamic viscoelastic responses. Fluorescence spectroscopic results of Luo et al.[10] on PTT cold crystallization revealed the formation of local dimers (parallel arrangement of two neighboring PTT chains) in the induction period prior to crystallization, which subsequently evolved into crystalline nuclei and then small crystallites. A four-stage process of induction, nucleation, growth, and late-stage crystallization was proposed. Very recently, the four-stage PTT cold crystallization was further examined by simultaneous small/wide-angle X-ray scattering (SAXS/WAXS) and dielectric spectroscopy[11] to correlate the evolution of PTT crystallinity and dielectric strength as an attempt to elucidate the formation of rigid amorphous phase during the cold crystallization process; structural evolution before crystallization, however, was not fully addressed.

Preordering prior to polymer crystallization has been revealed and discussed for sometime based mainly on X-ray and/or light scattering results.[12−23] As the preordering behavior is beyond the scope of the classical model[24] for polymer crystallization that assumes preexisted crystalline surfaces for regulating chains' folding and attachment to the surfaces, different mechanisms based on mesomorphic phase formation,[15−17] or liquid-like phase separation[18−23] (via nucleation-and-growth, NG, or spinodal decomposition, SD, mechanisms) have been proposed to rationalize the large-scale ordering prior to crystal growth. The recently observed dimer formation prior to the cold crystallization of PTT favored the nucleation-and-growth process for chain preordering. Previously, we also suggested that the gelation behavior and the development of optical anisotropy could be related to chain preordering immediately before cold crystallization of PTT.[9]

Via enhanced time/spatial resolutions in synchrotron-based simultaneous SAXS/WAXS and differential scanning calorimetry (DSC) measurements, here we report the nucleation, growth, and percolation of mesomorphic domains (from a dimension of 18 to 50 nm) and the development of nanograins (of dimensions of several nanometers) within these mesomorphic domains in the course of cold crystallization of PTT at 55 °C. With complementary identification of *trans*-to-*gauche* conformation transition via time-resolved Fourier-transform infrared spectroscopy (FTIR), the formation of the mesomorphic domains is discussed in terms of an analogy to liquid−liquid phase separation whereas the subsequent crystallinity development within these mesomorphic

*To whom correspondence should be addressed. E-mail: weitsung@nsrrc.org.tw (W.-T.C.); usejng@nsrrc.org.tw (U.-S.J.); poda@mail.ntust.edu.tw (P.-D.H.).

 Published on Web 02/02/2011

domains is interpreted in terms of a nucleation-and-growth path of polymer crystallization. It appears that the present observations serve to link a variety of previously proposed models into a more complete picture of polymer crystallization under far-from-equilibrium conditions.

Experimental Section

The poly(trimethylene terephthalate) (PTT) sample, kindly supplied by Shell Chemical, has an intrinsic viscosity of 0.92 dL/g (60/40 phenol/tetrachloroethane, 160 °C), with glass transition temperature $T_g \approx 45$ °C and melting temperature $T_m \approx 230$ °C. Glassy amorphous specimens (ca. 1 mm in thickness and 6 mm in diameter) were prepared by melt-pressing at 280 °C for 5 min before quenching into ice−water.

Simultaneous SAXS/WAXS/DSC measurements were performed at the 23A SWAXS beamline of the National Synchrotron Radiation Research Center (NSRRC).[25] The integrated setup was described in detail previously.[16] The specimen was placed in a Mettler Toledo FP84 DSC and isothermally crystallized at 55 °C for in situ SAXS/WAXS/DSC. The synchronized SAXS and WAXS data collection time was set to 1 frame per 15 s. With the incident beam ($\lambda = 1.550$ Å) offset from the center of the area detector MAR165-CCD for a wider SAXS q-range, the optimized geometry of the SAXS/WAXS/DSC setup covered the main WAXS reflections of PTT crystals in the q-range of 1.0−2.0 Å^{-1} and a SAXS q-range of 0.005−0.15 Å^{-1}. The corresponding sample-to-detector distances for the SAXS area detector and 1D WAXS detector (gas-type linear proportional counter) were 3100 and 600 mm, respectively. The scattering wavevector $q = 4\pi\lambda^{-1} \sin\theta$ (with scattering angle 2θ) was calibrated using silver behenate, sodalite, and silicon powder filled in a cell of 1 mm X-ray path length under the same PTT sample environment. Scattering data were routinely corrected for sample transmission, background, and detector sensitivity. SAXS intensity profiles $I(q)$ circularly averaged from the 2D images were placed on the absolute scale (defined as the differential scattering cross section per unit volume, in units of cm^{-1}).[26] With fresh specimens in repeated runs, experimental reproducibility was confirmed.

Time-resolved FTIR was performed on a glassy amorphous specimen during isothermal crystallization (Linkam hot stage at 55 °C), using a Thermo Nicolet 6700 Fourier transform infrared (FTIR) spectrometer equipped with a multichannel detector. The real-space image of the PTT sample at the end of crystallization was obtained using a Philips Tecnai G^2 F20 transmission electron microscope (TEM) operated under an accelerating voltage of 120 kV. The specimen ca. 70 nm in thickness was sectioned using a Leica Reichert Ultracut E ultramicrotome, followed by RuO_4 staining.

To extract the relative fractions of the amorphous, mesomorphic, and crystalline domains along the thermal annealing time, WAXS of nine PTT samples annealed at 55 °C for different lengths of time up to 4000 s were performed at the powder X-ray diffraction endstation of NSRRC beamline 01C (16 keV, $\lambda =$ 0.775 Å, and sample-to-detector distance = 296 mm). These same samples were further measured with temperature-modulated differential scanning calorimetry (TMDSC) using a Perkin-Elmer Diamond DSC under a dynamic mode with 60 s modulation period and 0.5 °C/min heating rate to extract the amorphous fractions of the samples (detailed below).

Data Analysis. SAXS intensity profiles in the low-q region (0.005−0.03 Å^{-1}) were modeled using the Guinier approximation

$$I(q) = I_0 \exp(-q^2 R_g^2/3) \quad (1)$$

for the radius of gyration R_g of the scattering particles (corresponding to the large mesomorphic domains in this study).[27] Here, $I_0 = n_p(\Delta\rho V)^2$ is a prefactor depending on the scattering particle concentration n_p, the particle volume V, and scattering contrast $\Delta\rho$.[9] SAXS intensity profiles in the intermediate-to-high-q region (0.04−0.2 Å^{-1}) contributed mainly by small PTT crystallites were modeled by $I(q) = n_p P(q) S(q)$, using the disk form factor $P(q)$ and a hard-sphere structure factor $S(q)$. For disks of thickness L and radius R, averaged over random spatial orientations[27]

$$P(q) = 16(\pi R^2 L)^2 \Delta\rho^2 \int_0^1 \left[\frac{J_1(qR\sqrt{1-x^2}) \sin(qLx/2)}{q^2 R\sqrt{1-x^2} Lx}\right]^2 dx \quad (2)$$

where J_1 is the Bessel function of the first order. In the Percus−Yevick (PY) expression,[28−30] the structure factor of hard spheres

$$S(q) = 1/[1 + 24\phi G(A)/A] \quad (3)$$

is defined by the volume fraction ϕ and the effective hard-sphere diameter d, with $A = qd$ and

$$G(A) = \frac{\alpha}{A^2}(\sin A - A\cos A) + \frac{\beta}{A^3}[2A\sin A + (2-A)^2\cos A - 2] + \frac{\gamma}{A^5}\{-A^4\cos A + 4[(3A^2-6)\cos A + (A^3-6A)\sin A + 6]\} \quad (4)$$

where $\alpha = (1+2\phi)^2/(1-\phi)^4$, $\beta = -6\phi(1+\phi/2)^2/(1-\phi)^4$, and $\gamma = 0.5\phi(1+2\phi)^2/(1-\phi)^4$. The mean distance ξ of the particles can be deduced from n_p determined by the volume fraction and the hard sphere size.[16]

Electron density heterogeneity was evaluated in terms of the scattering invariant $Q_{SAXS} = \int_0^\infty I(q) q^2 dq$ based on a two-phase approximation.[27] In practice, the upper and lower limits of the integration were replaced by high-q and low-q bounds of SAXS profiles extrapolated for relative scattering invariant. DSC-determined crystallinity $W_{c,DSC}$ was extracted from the DSC trace based on the integrated heat flow up to time t and was normalized to the heat of fusion of perfect crystal $\Delta H_f^\circ =$ 140 J/g;[4] WAXS-determined crystallinity $W_{c,WAXS}$ obtained from the integrated intensity over the observed Bragg reflections (after subtraction of the amorphous intensity) was normalized by the integrated intensity over the total WAXS profile.

Results

Simultaneous SAXS/WAXS/DSC. Figure 1 show the SAXS profiles collected over the whole PTT cold crystallization process, which is divided into the four stages of (1) induction (Figure 1a), (2) nucleation (Figure 1b), (3) growth/crystallization (Figure 1c), and (4) ripening (Figure 1d), according to the distinctly different scattering features. All the data are subtracted from the profile measured for the glassy amorphous specimens at the beginning of the isothermal annealing ($t = 0$ at 55 °C). The profile of a monotonically decreased intensity with q is often observed in supercooled polymer melts,[31,32] which is of no direct relevance in this study. The SAXS profiles before removing the common background scattering are given as insets of Figure 1. Concomitantly obtained WAXS spectra and DSC trace are presented in Figure 2a,b.

In Figure 1a for the first 300 s of isothermal crystallization, growth of SAXS intensity with a form-factor-like scattering profile in the very low q region (0.005−0.04 Å^{-1}) reveals the formation of large, dispersed domains in the system.[27] Nevertheless, this period of time is assigned as the induction stage of crystallization, as there were little activities in DSC and WAXS traces (Figure 2) other than a trace amount of heat flow near the end of this stage. In the subsequent time interval of 300−600 s, SAXS intensity (Figure 1b) increased quickly in the low-q region around 0.01 Å^{-1}, signifying a

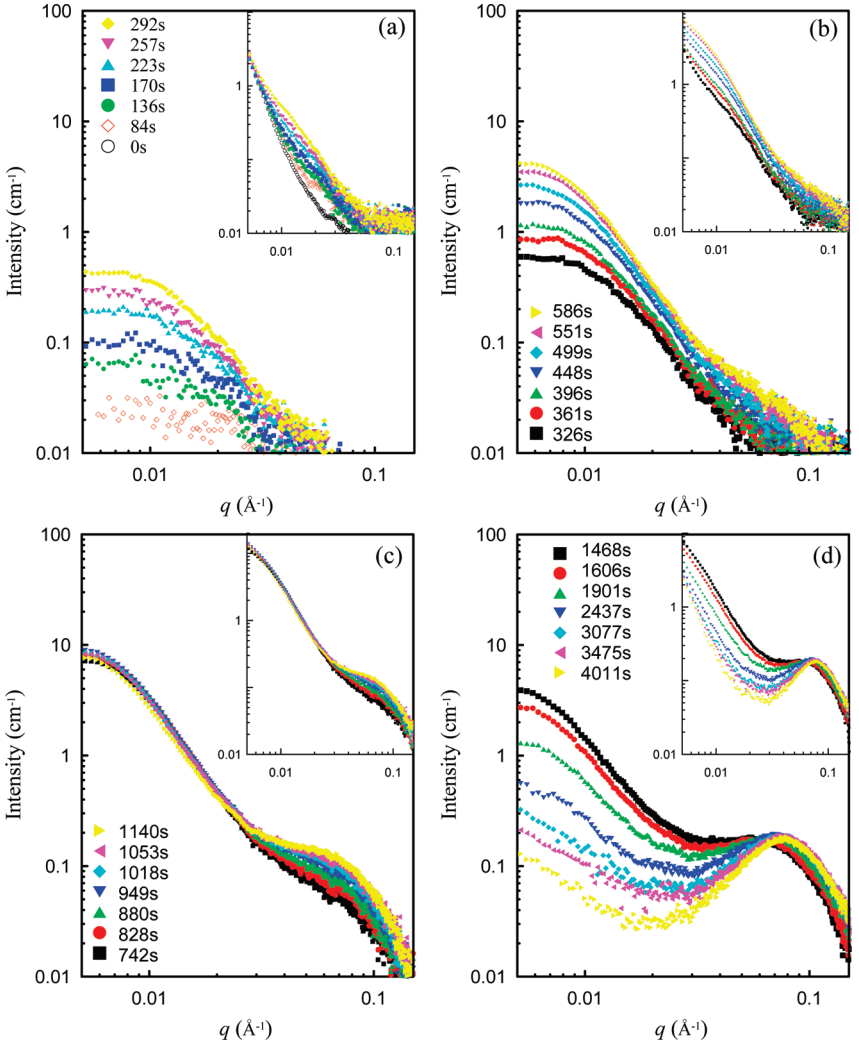

Figure 1. Time-resolved SAXS profiles with and without (insets) subtraction of the first featureless profile measured at the beginning of the isothermal crystallization at 55 °C. The profiles are divided into four stages (a−d) according to their distinctive scattering features.

drastic development of the mesomorphic domains. Meanwhile, the gradually increased intensity in the higher-q region ($q > 0.025$ Å^{-1}) revealed the development of small nanostructure corresponding to nucleation of nanograins (as suggested by the SAXS data analysis detailed below). This stage, thus termed as the nucleation stage, involved substantial exothermic activity (Figure 2b). Featureless WAXS spectra in Figure 2a, however, suggest that these small nanograins are of a noncrystalline entity.[16,17]

In the following period of $t = 600-1200$ s (Figure 1c), the seemingly saturated scattering intensity in the low-q (< 0.03 Å^{-1}) region implies matured mesomorphic domains. In contrast, fast increase in SAXS intensity in the higher-q region of 0.03−0.12 Å^{-1} corresponds to an active growth of the nanograins; the shoulder peak around $q \approx 0.06$ Å^{-1}, revealing formation of a short-range ordering of the nanograins due presumably to the significantly increased nanograins (in size and number density; detailed below). Concomitantly, broad Bragg's reflections in WAXS profiles (Figure 2a) and high activity in the DSC trace (Figure 2b) indicated that these nanograins grew largely and formed 3D organized chain packing, i.e., crystallization, in this growth/crystallization stage.

In the last stage of the isothermal crystallization ($t = 1200-4000$ s), the shoulder peak at ~0.06 Å^{-1} transits to a broad hump centered around 0.08 Å^{-1} (Figure 1d), implying an enhanced ordering of the nanocrystallites with a decreased mean spacing from 11 to 8 nm, as estimated from the Bragg law. Correspondingly, drastically improved WAXS reflections shown in Figure 2a indicated highly developed 3D chain packing; this involved, however, only residual exothermic activity (Figure 2b). Meanwhile, the low-q scattering intensity contributed mainly by mesomorphic domains decreased successively, which might be resulted from clustering of mesomorphic domains into agglomerates. Interconnected domains, of an extended correlation length but reduced scattering interfaces, may lead to the shifting of the scattering profile toward even lower q region and reduced scattering intensity in the monitored q region. A representative TEM image taken for a fully cold crystallized PTT sample at 55 °C supports the clustering of large mesomorphic domains (the bright domains in Figure 3a) into multiply connected agglomerates; the small PTT nanocrystallites inside the mesomorphic domains, however, were not observable from the TEM image due to the lack of sufficient contrast. Correspondingly, a bluish haze from the crystallized sample (Figure 3b) indicates existence of characteristic lengths in the range of several hundred nanometers, presumably from the agglomerates.

Time-Resolved FTIR. Shown in Figure 4a are the time-resolved FTIR spectra recorded over the PTT cold crystallization at 55 °C. Systematic changes of the several characteristic

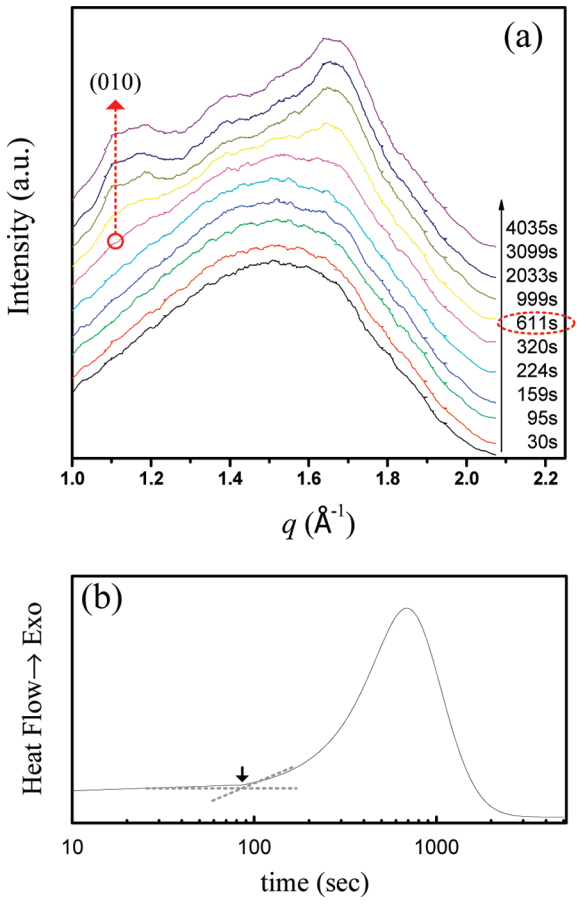

Figure 2. (a) Representative WAXS profiles and (b) the corresponding DSC trace simultaneously obtained along with the SAXS profiles (Figure 1) during cold crystallized of PTT at 55 °C. The arrow in (a) denotes development of WAXS-detectable crystallinity after $t = 600$ s, whereas that in (b) marks the onset of the crystallization exotherm at $t = 90$ s. Note that the logarithmic t scale tends to visually exaggerate the weighting of thermal activity in the short-t range.

absorption peaks in the region of 800−1000 cm^{-1} could be observed during the crystallization development. The net absorbance changes (Figure 4b), after subtracting out that contributed by the initial state prior to the isothermal crystallization, illustrate better the growth in the bands centered at 871, 935, and 948 cm^{-1}, and the decay in the bands centered at 874, 815, and 978 cm^{-1} during the crystallization process. In previous studies,[33,34] the 871 and 874 cm^{-1} bands were associated with the B_{3u}-CH out-of-plane bending of the phenylene rings in the crystalline and amorphous phases, respectively, and the 978 cm^{-1} band with the vibration of trans glycol segments. On the other hand, the 948 and 935 cm^{-1} bands were related to the CH_2 rocking of glycol residues in a *gauche* conformer in the crystalline phase, whereas the 815 cm^{-1} band to the same group but in a *trans* conformer in the amorphous phase. The absorbance changes in these bands observed (Figure 4b) are in general consistent with the *trans*-to-*gauche* transition behavior in PTT cold crystallization,[35] as illustrated by the prominent decay and growth of the 815 and 935 cm^{-1} bands, respectively, along the annealing time in Figure 4c.

Complications arise in quantitatively correlating the absolute gauche content in the system to the absorbance measured, as local environments of the CH_2 rocking of glycol residues of the two conformers are different. Nevertheless, following the previous assumption by Chuah,[36] we could estimate a relative *gauche* content $G(t) = A_{935}/(A_{935} + A_{815})$ defined by the respective normalized (to unity) absorbance

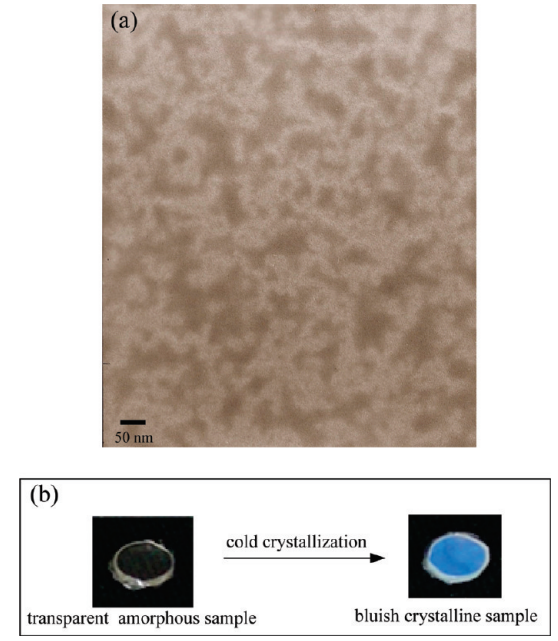

Figure 3. (a) TEM bright-field image of the PTT after cold crystallization at 55 °C, demonstrating percolated crystalline domains within the RuO_4-stained amorphous matrix (dark area). (b) Photographs illustrating the change from transparency of the as-quenched PTT glass to translucency (with bluish tints) after cold crystallization.

bands $A_{935}(t)$ and $A_{815}(t)$ at 935 and 815 cm^{-1}.[36] As shown in Figure 4c, $G(t)$ increases from 0.28 in the beginning of the nucleation stage ($t \approx 300$ s) to 0.41 at the end of the crystallization. This result indicates that the local *trans*-to-*gauche* transition in chain conformation started to occur only after formation of the mesomorphic domains in the induction stage I and was associated closely with the formation and crystallization of nanograins in the subsequent stages.

Correlated Structural Characteristics. We performed detailed data analysis to correlate the SAXS, WAXS, and DSC results quantitatively. For the mesomorphic domain size, we modeled the SAXS profiles (Figure 5) in the low-q region with the Guinier approximation.[27,37] The fitting result summarized in Figure 7 indicates that the mesomorphic domains have a nucleation size of $R_g \approx 7$ nm (diameter $D \approx 18$ nm, if spherical shape is assumed). The size then grows steadily according to $R_g \propto t^{0.5}$ up to 20 nm (or $D \approx 50$ nm for spheres) at the end of the growth/crystallization stage. Fitting results using sphere form factor and Schultz size distribution function[17,27] indicate that the polydispersity of the mesomorphic domains enlarges from 9 to 15% when the diameter increases from 18 to 50 nm.

On the other hand, we modeled the SAXS data in the higher q (0.04−0.16 $Å^{-1}$) region using disk geometry for the nanograins; sphere and rod models could not fit the data satisfactorily, whereas oblate shape gave similar result to that given by the disk model. In the nucleation and growth stages, simple form factor $P(q)$ could fit the data reasonably well (Figure 6); PY hard-sphere structure factor $S(q)$ had to be used in the late stage of crystallization, as illustrated in Figure 6. The growths of the fitted disk diameters $2R$ (2.5−5.0 nm) and thickness L (2.2−3.0 nm) and the nearly constant mean spacing of the nanograins ξ (decreased from 8 to 7 nm) are summarized in Figure 7. The fitted thicknesses (L) of the disk-like nanocrystallites are, in general, consistent with those obtained using the 1D correlation function analysis for the crystal slab thickness.[9] The nanograins of aspect ratio $2R/L = 1.5$ and mean spacing 7 nm may be taken as

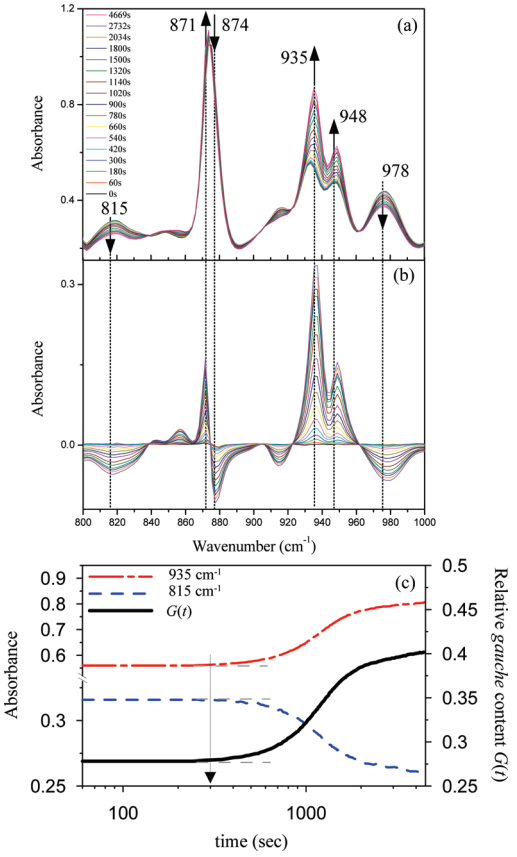

Figure 4. (a) Time-resolved FTIR spectra of PTT, (b) the difference spectra after subtraction of the first spectrum measured at $t = 0$, and (c) normalized absorbance changes in 935 and 815 cm^{-1} bands and increase in FTIR-determined relative *gauche* content $G(t)$ during cold crystallization at 55 °C.

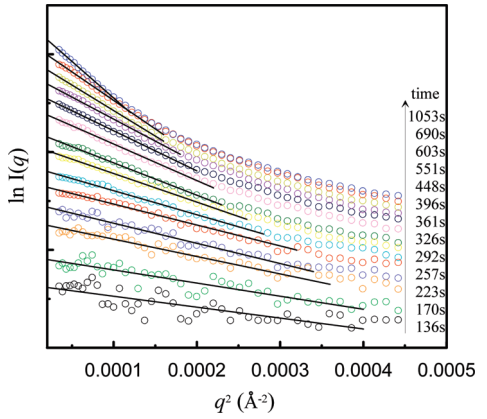

Figure 5. Guinier plots of the SAXS data and the corresponding fittings (solid lines).

imperfectly stacked lamellae (near-neighbor ordered in a range of ~20 nm, as estimated from the width of the scattering hump). To correlate all the activities during the crystallization process, we have also included normalized crystallinities $W_{c,WAXS}$ and $W_{c,DSC}$ as well as scattering invariant Q_{SAXS} (extracted from the WAXS, DSC, and SAXS data) in Figure 7.

Discussion

Preordering Behavior. Previously, on the basis of simultaneous SAXS/WAXS/DSC results, we proposed formation of

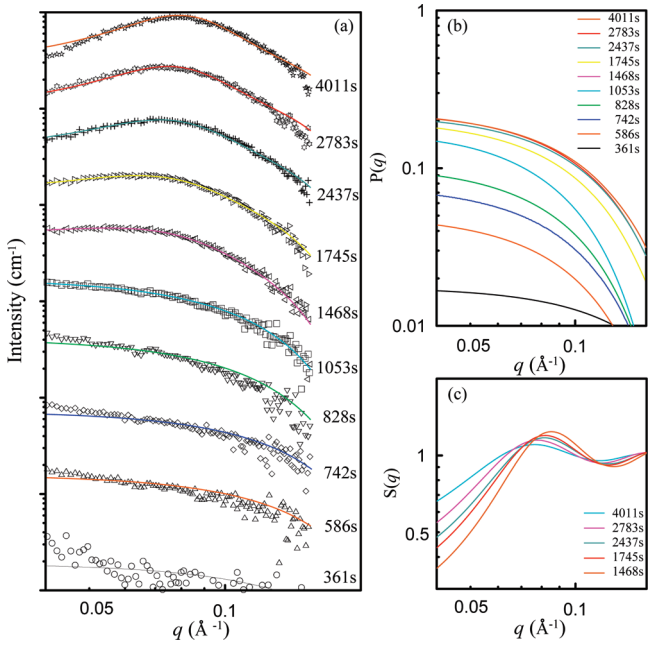

Figure 6. (a) Model-fitting (solid curves) of the SAXS profiles (subtracted with the featureless profile measured before isothermal annealing) in the high-q region. (b) The best-fit disk form factor $P(q)$. (c) The corresponding PY structure factor $S(q)$.

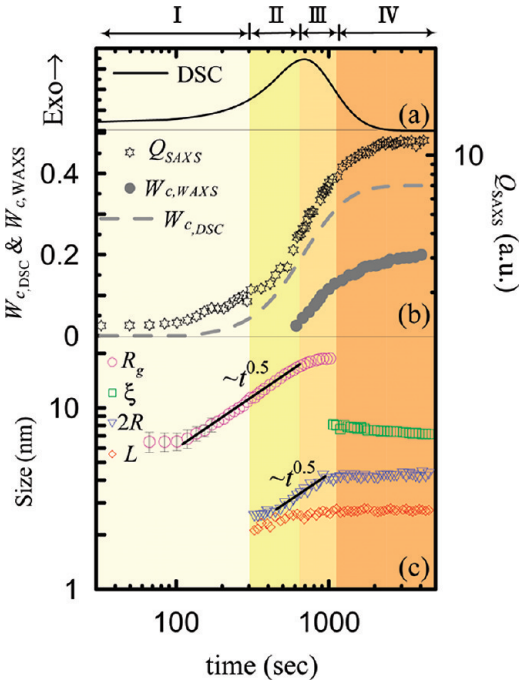

Figure 7. Structural evolution during cold crystallization of PTT: (a) DSC trace, (b) development of DSC- and WAXS-defined crystallinities $W_{c,DSC}$ and $W_{c,WAXS}$, and SAXS invariant Q_{SAXS}, (c) radius of gyration of the mesomorphic domains R_g, diameter ($2R$) and thickness (L) of the disk-like nanocrystalline grains within the mesomorphic domains, and mean spacing ξ between neighboring nanograins. Different background shades indicate the four assigned stages of (I) induction, (II) nucleation, (III) growth/crystallization, and (IV) ripening.

noncrystalline nanograins prior to crystallization based on the cold crystallization of poly(9,9-di-*n*-octyl-2,7-fluorene) (PFO)[16] and syndiotactic polystyrene (sPS).[17] There, we also commented[16] on similarities and differences of the proposed nanograin picture as compared to earlier concepts of

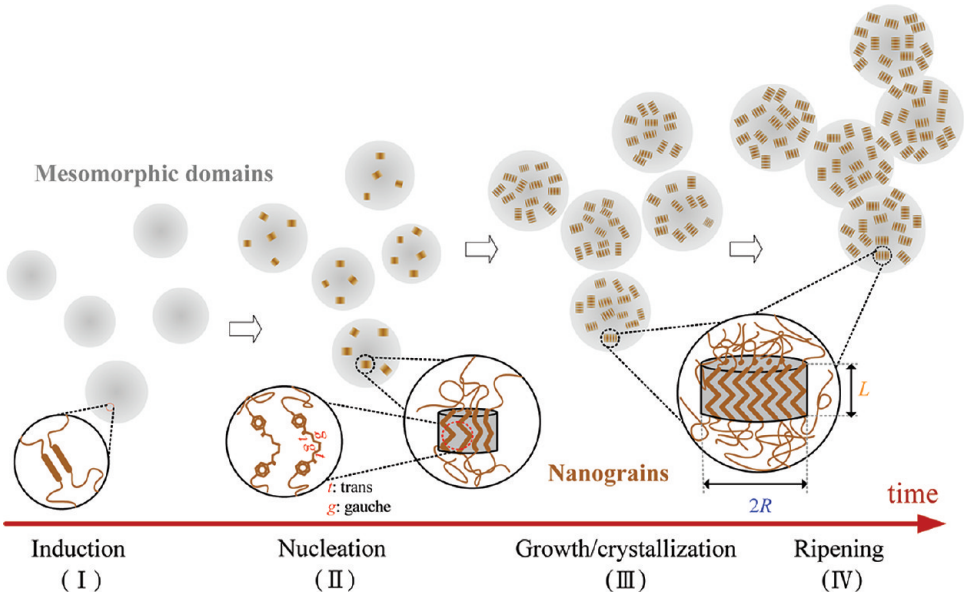

Figure 8. Schematic illustration of the proposed evolution of hierarchical structure during cold crystallization of PTT at 55 °C: (I) mesomorphic domains containing short-range aligned chains (dimers) for the induction stage, (II) mesomorphic domains with noncrystalline nanograins inside for the nucleation stage, (III) loosely interconnected mesomorphic domains, each filled with crystallized nanograins for the growth stage, and (IV) multistage agglomerates comprised of the percolated network of mesomorphic domains filled with nanograins during final ripening.

nanocrystalline blocks by Perterlin,[38] mesomorphic precursor by Strobl,[15] and spinodal-like cold crystallization mechanism by Ryan in particular.[22] In those comments, we related the solid-like molecular packing, the lack of crystal-like reflections, and the stagnant size without growth of the nuclei (nanograins) to the "mesophase" precursor hypothesized by Strobl and indicated that such NG behavior bears no direct counterpart in SD mechanism.

In this study with PTT cold crystallization, we furthermore unveiled an even earlier and larger scale of chain preordering behavior (tens of nanometers), i.e., the formation of large mesomorphic domains, before formation of small noncrystalline nanograins (a few nanometers), as illustrated in Figure 7. Monotonic intensity increase of the SAXS profile without an ordering peak in the low-q region prior to crystallization was also observed by Imai and Kaji on the crystallization of a homologous polymer of poly(ethylene terephthalate) (PET).[20] On the basis of the liquid−liquid phase separation mechanism proposed by Olmstead et al.,[39] this phenomenon was interpreted as NG of large mesomorphic domains (termed as "droplets" therein)[20] resulted from a primary phase separation of the polymer melt in the metastable region upon cooling to some 20 °C below the melting temperature T_m. Moreover, the oriented (smectic) domains subsequently observed before formation of smaller crystallites inside these mesomorphic domains from the primary phase separation (the so-called SAXS peak prior to WAXS reflections[20,22]) was then described as the secondary phase separation via spinodal decomposition.

Summarized in Figure 7 are characteristics for the large mesomorphic domains we observed in the induction stage of PTT cold crystallization. The lack of crystal-like reflections, the stagnant domain size for a short moment (up to $t \approx 100$ s) before growth, the conservation of the *trans*/*gauche* composition (Figure 4c), and the formation of mesomorphic domains in a large scale before crystallization are qualified for phase separation via a mechanism similar to that proposed previously based on the coupling between density and chain conformation.[20,22,39] It is then appealing to follow the interesting theoretical frame devised by Ryan et al.[22] for phase separation and relate the two conformers of *trans* and *gauche* of PTT to the two

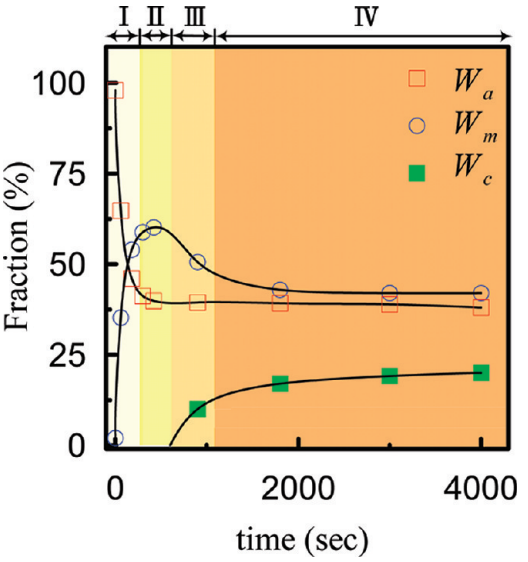

Figure 9. Evolutions of the fractions of amorphous (W_a), mesomorphic (W_m), and crystalline domains (W_c) during PTT cold crystallization at 55 °C. The solid curves are for eye-guiding only. Different background shades indicate the four assigned stages of (I) induction, (II) nucleation, (III) growth/crystallization, and (IV) ripening.

components needed in the phase separation; the conserved population of the conformers observed in the induction stage I simply fits the assumption required for the phase separation. Furthermore, using small-angle light scattering (SALS),[9] we have observed previously the occurrence ($t \approx 100$ s) of optical anisotropy in the induction stage, due presumably to a consequence of chain orientation fluctuations/segregation (for a nematic-like ordering), that relates to the assumed key driving force of density−conformation coupling in this phase separation mechanism for homopolymer crystallization.[22,39] No nematic-like domains, however, could be identified in that study with SALS,[9] presumably due to the relatively small mesomorphic domains size of several tens of nanometers (as revealed by SAXS here), relative to the sensitive length scale of the optical

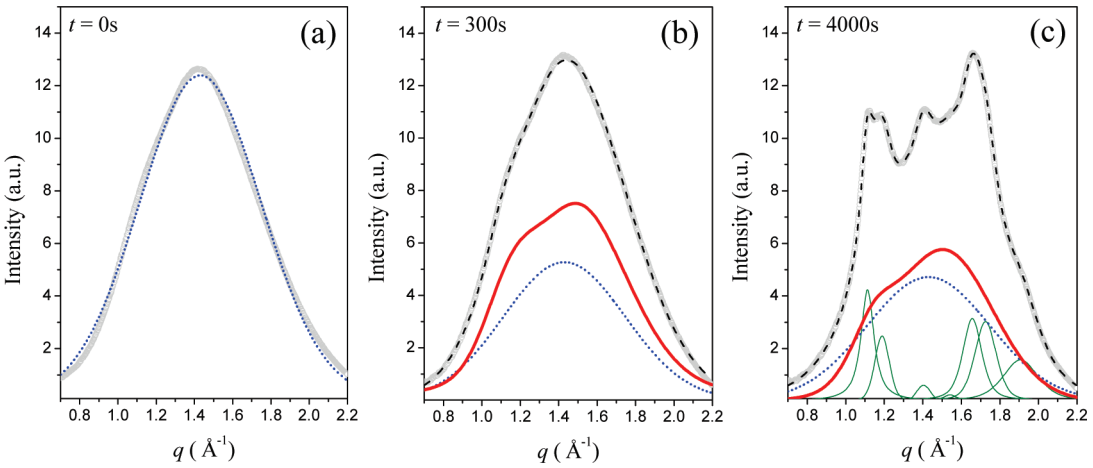

Figure 10. Selected WAXS profiles of an as-quenched PTT sample (a) and samples annealed at 55 °C for (b) 300 s and (c) 4000 s. The WAXS data (open circle) are respectively fitted with the amorphous halo (dotted line) in (a), and the mesomorphic (thick solid curve) and amorphous (dotted curve) halos in (b), and seven crystalline peaks (thin solid curves) together with the reduced mesomorphic (solid curve) and amorphous (dotted curve) halos in (c).

tool used. Note that phase separation may occur via the route of either NG or SD, depending on, for instances, the initial conformer composition or the crystallization temperature.[20] We speculate that the asymmetric relative *gauche* content of 0.28 (Figure 4c) might be a critical parameter for the NG route observed for PTT. More experimental data with different conformer ratios (which may be modulated by annealing temperature, crystallization temperature, or mechanical orientation such as shearing), however, are needed to clarify this speculation. Interestingly, with dynamic mechanical analysis,[9] we could determine a gelation point near the transition from the induction to nucleation stage. The gelation point implies a liquid-to-solid transition behavior and signifies the beginning of the formation of noncrystalline nuclei of solid-like molecular packing.

Nanograin Crystallization Behavior. Subsequent to the phase separation for mesomorphic domains are the high local chain activities, include formation of the noncrystalline PTT nanograins in the nucleation stage II, growth/crystallization of the nanograins in stage III and the final matured crystallites with a short-range ordering in stage IV. Other than some details depending on the specific properties of PTT, the structural evolution of the nanograins within presumably the large mesomorphic domains, in general, follows the nanograin model we proposed previously for the cold crystallizations behavior of PFO[16] and sPS.[17]

The time-resolved FTIR result further elucidates that the onset of chain conformation transition, namely, the trans-to-gauche transition (Figure 4c), was concomitant with nucleation of the small noncrystalline nanograins in stage II (Figure 7c), which involved a high activity of the exothermic trace prior to the detection of WAXS reflections (for 3D ordered chain packing) in the growth stage III. Quantitative analysis indicates that ca. 40% (Figure 7b) of the total heat release occurred in stage II for the formation/growth of the noncrystalline nanograins. Including the heat flow in the induction stage I, chain preordering behavior prior to crystallization contributed as much as 50% of the total heat release in the whole crystallization process. The nucleation of the noncrystalline nanograins is manifested by the stationary size for a short moment before the growth of the nanograins in both the lateral size ($2R$) and thickness (L) of the disk-like morphology (Figure 7c).

In the subsequent stage III for major crystallization, only the lateral size of the nanograins grew continuously, which accompanied the fast development of WAXS reflections from this preferred crystallization plane perpendicular to the molecular axis of the disk-like nanograins. The growth rate of the lateral size of the nanograins follows roughly a power-law behavior of $t^{0.5}$, suggesting a diffusion-controlled growth mechanism, which may be suitable for ordered chains diffusing within a random-chain-confined matrix. The growth stage III manifests high activities in the SAXS invariant (Q_{SAXS}) and the DSC and WAXS defined crystallinities ($W_{c,WAXS}$ and $W_{c,DSC}$), as shown in Figure 7a,b. Overall, stage III contributed another 40% of the total heat flow and the first 15% of crystallinity (out of the 22% total crystallinity). The much earlier development of $W_{c,DSC}$ than that of $W_{c,WAXS}$ reveals a comparable heat flow contribution from noncrystalline chain preordering in stages I and II, as compared to that released from organizing 3D ordered chains of WAXS reflections in stages III and IV.

The final stage IV for ripening is marked by the emergence of a mean spacing ξ owing to the formation of a short-range ordering of PTT crystallites (Figure 7). The slowly decreased ξ in this stage implies asymptotically saturated number density and size of the crystallites, leading to the residual activities of Q_{SAXS}, $W_{c,DSC}$, and $W_{c,WAXS}$. The size of the mesomorphic domains can no longer be determined from the SAXS profiles during this stage, as these domains had collided with each other into agglomerates evidenced by TEM (Figure 3), hence losing the entity of individual size. Fusion of these mesomorphic domains for agglomerates may, in some sense, terminates the growth/expansion of the PTT nanocrystallites inside, leading to denser, short-range ordered nanocrystallites.

In Figure 8, we cartoon the structural features of each stage in the PTT cold crystallization, including (I) mesomorphic domains that are rich in short-range aligned chains (dimers) for the induction stage, (II) noncrystalline nanograins populated inside the dispersed mesomorphic domains for the nucleation stage, (III) loosely interconnected mesomorphic domains, each filled with crystallized nanograins for the growth stage, and (IV) the multistage agglomerates comprised of the percolated network of mesomorphic domains filled with short-range ordered crystallites for the final ripening stage. It is then interesting to note that, as the mesomorphic domain morphology places possible restrictions to the final crystallite size and morphology, controlled phase separation via proper selections of quenching/annealing conditions offers

possibilities of manipulating subsequent crystallization kinetics and gelation behavior. This awaits further scrutiny.

Transitions among Amorphous, Mesomorphic, and Crystalline Domains. We have interpreted the cold crystallization of PTT in terms of the evolutions of the mesomorphic domains and crystalline nanograins; the corresponding structure characteristics revealed by SAXS, including the domains size and shape, are manifested in Figures 7 and 8. Furthermore, we show below the local chain packing characteristics of the amorphous, mesomorphic, and crystalline phases via their signature WAXS patterns as well as the characteristic transitions between these phases during thermal annealing. Using the WAXS profiles collected for the PTT samples annealed at 55 °C for different lengths of time (cf. Figure 9), we could decompose the fractions of the three phases. Specifically, the crystalline fractions of these annealed samples were calculated from the WAXS-determined crystallinity W_c as that done previously. On the other hand, the corresponding amorphous fractions of the samples were extracted from the scaling relation $W_a = \Delta C_p/\Delta C_p^{\circ}$, where ΔC_p is the heat capacity increment at T_g measured using TMDSC, and $\Delta C_p^{\circ} = 94$ J K^{-1} mol^{-1} corresponds to the heat capacity increment of a complete amorphous phase reported previously.[40] Here, we have assumed that mesomorphic domains do not contribute significantly to ΔC_p. With the fractions of the crystalline and amorphous phases determined, the fractions of the mesomorphic domains W_m in these samples could be straightforwardly deduced based on the unity conservation. The thus-extracted fractions of the amorphous, mesomorphic, and crystalline phases along the annealing time are illustrated in Figure 9. Correlated evolutions of these fractions indicate that (i) the transition from amorphous domains to mesomorphic ones occurred mainly in the induction stage I and saturated to ~60% in the stage II and (ii) the growth of the 20% crystalline domains in stages III and IV was transformed mainly from the mesomorphic domains, while the amorphous domains remained at a constant fraction. The ~40% mesomorphic domains left at the end of the PTT cold crystallization at 55 °C ($t = 4000$ s in Figure 9), likely corresponds to the rigid-amorphous phase proposed previously.[40] Complete transformation of the mesomorphic to crystalline domains was observed in the cold crystallization of isotactic polypropylene (iPP) previously.[41]

With the determined fractions of the amorphous, mesomorphic, and crystalline phases (Figure 9), we could retrieve the signature WAXS pattern of the mesomorphic domains (Figure 10b) from the WAXS profile measured at $t = 300$ s (end of the stage I; only two phases involved), simply after removing the percentage contribution (40%) of the amorphous WAXS profile (Figure 10a) measured at $t = 0$ s. Similarly, the WAXS profile measured the end of cold crystallization (at $t = 4000$ s) could be decomposed into the reduced amorphous and mesomorphic halos, together with the seven characteristic crystalline peaks of PTT emerged (Figure 10c), according to the determined fractions 0.38, 0.42, and 0.2 for the amorphous, mesomorphic, and crystalline phases (Figure 9).

Conclusions

We have investigated the structure evolution of PTT in cold crystallization using simultaneous SAXS/WAXS/DSC, time-resolved FTIR, and TEM. Integration of the reciprocal- and real-space data allows us to construct a model of hierarchical structure evolution for the cold crystallization process, which comprises (I) induction, (II) nucleation, (III) growth/crystallization, and (IV) final ripening stages. A phase separation mechanism is adopted to describe the nucleation-and-growth of mesomorphic domains (with a linear dimension from 18 to 50 nm) in stages I to III. This is accompanied or followed by formation of nuclei and their subsequent development into crystalline nanograins up to several nanometers in the lateral (5 nm) and thickness (3 nm) dimensions in stages II to IV. Quantitatively resolved transitions among the amorphous, mesomorphic, and crystalline domains imply that the crystalline domains were developed mainly from the mesomorphic domains.

Acknowledgment. Financial support from the National Science Council (Grants NSC 99-2218-E-213-001-MY3 and NSC 99-2112-M-213-002-MY3) is gratefully acknowledged.

References and Notes

(1) Chuah, H. H. *Chem. Fibers Int.* **1996**, *46*, 424–428.
(2) Brown, H. S.; Chuah, H. H. *Chem. Fibers Int.* **1997**, *47*, 72–74.
(3) Hwo, C.; Brown, H.; Casey, P.; Chuah, H.; Dangayach, K.; Forschner, T.; Moerman, M.; Oliveri, L. *Chem. Fibers Int.* **2000**, *50*, 53–56.
(4) Chuang, W. C.; Yeh, W. J.; Hong, P. D. *J. Appl. Polym. Sci.* **2002**, *83*, 2426–2433.
(5) Hong, P. D.; Chuang, W. T.; Hsu, C. F. *Polymer* **2002**, *43*, 3335–3343.
(6) Hong, P. D.; Chuang, W. T.; Yeh, W. J.; Lin, T. L. *Polymer* **2002**, *43*, 6879–6886.
(7) Chuang, W. T.; Hong, P. D.; Chuah, H. H. *Polymer* **2004**, *45*, 2413–2425.
(8) Ho, R. M.; Ke, K. Z.; Chen., M. *Macromolecules* **2000**, *33*, 7529–7537.
(9) Chuang, W. T.; Hong, P. D.; Shih, K. S. *Polymer* **2004**, *45*, 8583–8592.
(10) Luo, W.; Liao, Z.; Yan, J.; Li, Y.; Chen, X.; Mai, K.; Zhang, M. *Macromolecules* **2008**, *41*, 7513–7518.
(11) Sanz, A.; Nogales, A.; Ezquerra, T. A.; Soccio, M.; Munari, A.; Lotti, N. *Macromolecules* **2010**, *43*, 671–679.
(12) Akpalu, A.; Kielhorn, L.; Hsiao, B. S.; Stein, R. S.; Russell, T. P.; van Egmond, J.; Muthukumer, M. *Macromolecules* **1999**, *32*, 765–770.
(13) Wang, Z. G.; Hsiao, B. S.; Sirota, E. S.; Agarwal, P.; Srinivas, S. *Macromolecules* **2000**, *33*, 978–989.
(14) Hikosaka, M.; Watanabe, K.; Okada, K.; Yamazaki, S. *Adv. Polym. Sci.* **2005**, *191*, 137–186.
(15) Strobl, G. *Eur. Phys. J. E* **2000**, *3*, 165–183.
(16) Su, C. H.; Jeng, U. S.; Chen, S. H.; Lin, S. J.; Ou, Y. T.; Chuang, W. T.; Su, A. C. *Macromolecules* **2008**, *41*, 7630–7636.
(17) Su, C. H.; Jeng, U. S.; Chen, S. H.; Lin, S. J.; Wu, W. R.; Chuang, W. T.; Tsai, J. C.; Su, A. C. *Macromolecules* **2009**, *42*, 6656–6664.
(18) Imai, M.; Mori, K.; Mizukami, T.; Kaji, K.; Kanaya, T. *Polymer* **1992**, *33*, 4451–4455.
(19) Imai, M.; Mori, K.; Mizukami, T.; Kaji, K.; Kanaya, T. *Polymer* **1992**, *33*, 4457–4462.
(20) Kaji, K.; Nishida, K.; Kanaya, T.; Matsuba, G.; Konishi, T.; Imai, M. *Adv. Polym. Sci.* **2005**, *191*, 187–240.
(21) Terrill, N. J.; Fairclough, P. A.; Towns-Andrews, E.; Komanschek, B. U.; Young, R. J.; Ryan, A. J. *Polymer* **1998**, *39*, 2381–2385.
(22) Ryan, A. J.; Fairclough, J. P. A.; Terrill, N. J.; Olmsted, P. D.; Poon, W. C. K. *Faraday Discuss.* **1999**, *112*, 13–29and references cited therein .
(23) Heeley, E. L.; Maidens, A. V.; Olmsted, P. D.; Bras, W.; Dolbnya, I. P.; Fairclough, J. P. A.; Terrill, N. J.; Ryan, A. J. *Macromolecules* **2003**, *36*, 3656–3665.
(24) Lauritzen, J. I.; Hoffman, J. D. *J. Res. Natl. Bur. Stand.* **1960**, *64A*, 73–102.
(25) Jeng, U. S.; Su, C. H.; Su, C. J.; Liao, K. F.; Chuang, W. T.; Lai, Y. H.; Chang, J. W.; Chen, Y. J.; Huang, Y. S.; Lee, M. T.; Yu, K. L.; Lin, J. M.; Liu, D. G.; Chang, C. F.; Liu, C. Y.; Chang, C. H.; Liang, K. S. *J. Appl. Crystallogr.* **2010**, *43*, 110–121.
(26) Lai, Y. H.; Sun, Y. S.; Jeng, U. S.; Lin, J. M.; Lin, T. L.; Sheu, H. S.; Chuang, W. T.; Huang, Y. S.; Hsu, C. H.; Lee, M. T.; Lee, H. Y.; Liang, K. S.; Gabriel, A.; Koch, M. H. J. *J. Appl. Crystallogr.* **2006**, *39*, 871–877.
(27) Feigin, L. A.; Svergun, D. I. *Structure Analysis by Small-Angle X-ray and Neutron Scattering*; Plenum: New York, 1987.
(28) Percus, J. K.; Yevick, G. J. *Phys. Rev.* **1958**, *110*, 1–13.
(29) Ashcroft, N. W.; Lekner, J. *Phys. Rev.* **1966**, *145*, 83–90.

(30) Kaler, E. N.; Bennett, K. E.; Davis, H. T.; Scriven, L. E. *J. Chem. Phys*. **1983**, *79*, 5673–5684.
(31) Fisher, E. W. *Physica A* **1993**, *201*, 183–206.
(32) Weber, H.; Paul, W.; Kob, W.; Binder, K. *Phys. Rev. Lett*. **1997**, *78*, 2136–2139.
(33) Ward, I. M.; Wilding, M. A. *Polymer* **1977**, *18*, 327.
(34) Kim, K. J.; Bae, J. H.; Kim, Y. H. *Polymer* **2001**, *42*, 1023–1033.
(35) Dandurand, S. P. *Polymer* **1979**, *20*, 419–426.
(36) Chuah, H. H. *Macromolecules* **2001**, *34*, 6985–6993.
(37) Jeng, U. S.; Liu, W. J.; Lin, T. L.; Wang, L. Y.; Chiang, L. Y. *Fullerene Sci. Technol*. **1999**, *7*, 599–608.
(38) Peterlin, A. *Text. Res. J*. **1972**, *42*, 20–27.
(39) Olmsted, P. D.; Poon, W. C. K.; McLeish, T. C. B.; Terrill, N. J.; Ryan, A. J. *Phys. Rev. Lett*. **1998**, *81*, 373–376.
(40) Pyda, M.; Wunderlich, B. *J. Polym. Sci., Part B: Polym. Phys*. **2000**, *38*, 622–631.
(41) Konishi, T.; Nishida, K.; Kanaya, T. *Macromolecules* **2006**, *39*, 8035–8040.